*fibers*

MDPI

*Article*

# Inverse-Analysis Identification of Material Parameters in Hybrid-Reinforced (Bars Plus Fibers) Concrete Beams Through the Updated Bridged Crack Model (UBCM)

**Bineet Kumar, Dongxi Xie * and Alberto Carpinteri**

College of Engineering, Shantou University, 243 Daxue Road, Jinping District, Shantou 515063, China; bineetkumar@stu.edu.cn (B.K.); alberto.carpinteri52@gmail.com (A.C.)
* Correspondence: dxxie@stu.edu.cn

## Highlights

**What is the main finding?**

- A staged inverse-analysis procedure based on the Updated Bridged Crack Model (UBCM) successfully identified effective matrix, fiber, and steel reinforcement parameters from seven calibration configurations, reproducing the principal flexural responses of nine independent hybrid-reinforced concrete configurations without further recalibration.

**What is the implications of the main finding?**

- The proposed approach enables the individual contributions of matrix cracking, fiber pull-out, and steel-bar yielding to be interpreted within a unified fracture-mechanics framework, providing a basis for identifying physically meaningful model parameters and predicting the response of different reinforcement combinations.

## Abstract

Hybrid-reinforced concrete (HRC) beams exhibit a complex flexural response governed by the interaction between matrix cracking, fiber pull-out, and steel-bar yielding, which complicates the identification of constituent properties from global load–deflection data. This study develops an inverse-analysis procedure based on the Updated Bridged Crack Model (UBCM), in which concrete matrix, discontinuous steel fibers, and longitudinal reinforcement are represented as mechanically distinct phases. An experimental database comprising 48 four-point-bending tests was considered. For transparent interpretation and parameter-sensitivity assessment, the identification was performed sequentially using plain-concrete, fiber-reinforced concrete, and reinforced-concrete specimens. Effective matrix modulus and fracture toughness, equivalent fiber pull-out force, critical pull-out displacement, and steel yield strength were identified from seven calibration configurations. A multi-objective optimization was employed for the fiber parameters by minimizing discrepancies in the maximum load and area under the load–deflection response. Further nine HRC configurations experimental results are used to validate the numerical predictions by UBCM. The UBCM reproduced first-cracking condition, post-cracking load recovery, fiber-controlled softening, and transition towards steel-controlled yielding. The results demonstrate that constituent properties governing HRC fracture can be identified and transferred while retaining their physical meaning and role.

**Keywords:** hybrid-reinforced concrete; inverse analysis; Updated Bridged Crack Model; material identification; fiber pull-out; fracture mechanics

Check for updates

Academic Editors: Marta Roig-Flores and David Hernandez Figueirido

Received: 17 October 2026
Revised: 1 November 2026
Accepted: 9 November 2026
Published: 16 November 2026

**Copyright:** © 2026 by the authors. Licensee MDPI, Basel, Switzerland. This article is an open access article distributed under the terms and conditions of the Creative Commons Attribution (CC BY) license.

## 1. Introduction

Hybrid-reinforced concrete (HRC) combines conventional longitudinal steel bars with discontinuous fibers randomly distributed within a cementitious matrix. The two reinforcing systems provide complementary resistance after cracking. Longitudinal bars bridge the dominant crack through bond transfer, elastic deformation and yielding, whereas fibers transfer stresses locally across the fracture process zone through debonding, mechanical anchorage and progressive pull-out. Their simultaneous action can improve crack control, post-cracking resistance, deformation capacity and energy dissipation [1–7]. Nevertheless, the flexural response of HRC cannot be interpreted as a simple superposition of reinforced concrete (RC) and fiber-reinforced concrete (FRC), because several mechanisms, including matrix cracking, fiber pull-out, steel-bar yielding, possible bar rupture and concrete crushing, may become active successively or simultaneously.

The interaction among these mechanisms is illustrated schematically in Figure 1. The initial branch $O - A$ represents the approximately linear response before formation of the dominant flexural crack. Point $A$ denotes the onset of matrix cracking, after which the tensile resistance previously provided by concrete rapidly decreases and the reinforcing phases become responsible for transferring stresses across the developing cracks (Figure 2).

For beams containing a low longitudinal reinforcement ratio, the steel bars alone may be unable to compensate immediately for the loss of tensile resistance associated with concrete cracking. In a corresponding RC beam, the response therefore approaches a relatively low yielding-controlled branch. In the HRC beam, fibers intersecting the fracture plane become progressively activated after Point $A$, transferring stresses between the crack faces and promoting recovery of the load along branch $A - B$. Point $B$ represents a condition in which the collective fiber contribution is highly mobilised. However, the fibers crossing the critical section are not all in the same mechanical state: some remain bonded to the surrounding matrix, some undergo debonding and straightening of their hooked ends, and others have already entered the pull-out stage. The measured response therefore reflects the combined action of fibers at different stages of mobilisation.

As the crack continues to open, the available embedded length of the fibers decreases and an increasing number of fibers are progressively extracted from the matrix. The gradual exhaustion of fiber bridging produces the descending branch $B - C$. The shape of this branch depends on the pull-out behaviour, anchorage, orientation and distribution of the fibers crossing the fracture plane. Fiber action is therefore not lost suddenly; instead, its contribution decreases progressively as different fibers complete the pull-out process at different crack openings.

At very low longitudinal reinforcement ratios, fibers may also improve crack control and enhance the local bond between the concrete and the steel bars. Although this effect generally increases the post-cracking load capacity, it may restrict the length over which plastic bar deformation can develop. Strain can consequently localize near the dominant crack, creating the possibility of premature bar rupture around Point $C$ [2,7]. Thus, fiber addition does not necessarily increase the ultimate deformation capacity of very lightly reinforced beams, even when it improves their post-cracking strength. When bar rupture does not occur and fiber bridging becomes progressively exhausted, the HRC response tends towards branch $C - D$, where the behaviour is governed mainly by yielding and continued deformation of the longitudinal reinforcement. The HRC curve consequently approaches the corresponding RC response because the remaining contribution of the fibers becomes comparatively small.

A different failure sequence develops when the longitudinal reinforcement ratio is larger. Following cracking at Point $A$, the continuous reinforcement can compensate for the reduction in tensile resistance of the matrix, allowing the load to continue increasing

along branch $A - E$. In this regime, the steel bars provide the dominant crack-closing action, while the relative influence of the fibers on the maximum load becomes less pronounced. Yielding of the longitudinal reinforcement produces the plateau $E - F$. At even larger deformations, failure may be governed by compression-side damage and concrete crushing. Compared with ordinary RC, fibers distributed within the compression zone restrain crack opening, fragmentation, and separation of the damaged concrete, producing a more gradual descending branch $F - G$ [3,7].

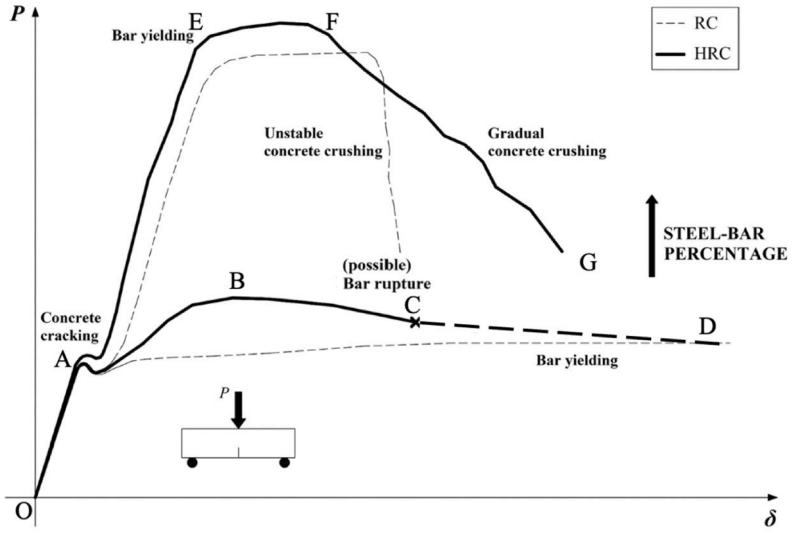



**Figure 1.** Load-deflection behaviour of HRC beam in case of under-reinforcement and over-reinforcement.

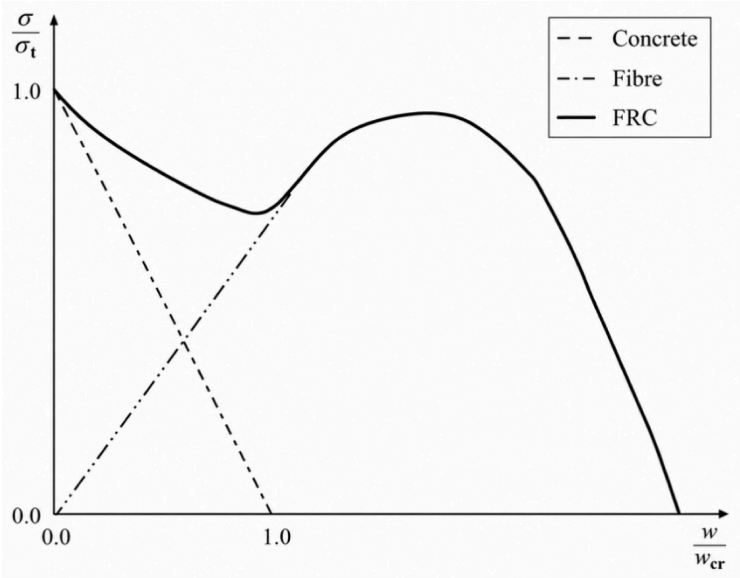



**Figure 2.** Cohesive law in FRC: Superposition of matrix and fiber-reinforcement contributions.

Figure 1 therefore demonstrates that the global load–deflection response of an HRC beam contains overlapping contributions from different fracture and reinforcement mechanisms. Their sequence and relative importance drastically depend on the combination of fiber content and longitudinal reinforcement. This interaction makes the interpretation of HRC behaviour more complex than that of plain concrete, FRC, or RC considered separately.

The fracture behaviour of cementitious materials is commonly described through cohesive relationships between tensile stress and crack opening. Since the fictitious-crack

formulation proposed by Hillerborg et al. [8], similar approaches have been widely used to represent progressive degradation within the fracture process zone [9–12]. For FRC, the corresponding constitutive law incorporates both the softening contribution of the matrix and the residual stress transferred by the fibers [13–16]. Because direct tensile characterization is experimentally demanding, such constitutive relationships are frequently obtained through inverse analysis of flexural tests. In these procedures, unknown constitutive parameters are varied until the numerical load–deflection or load–CMOD response reproduces the experimental curve [17–27].

Inverse-analysis techniques have been successfully applied to conventional concrete, FRC, and high-performance fiber-reinforced composites [28–33]. Depending on the adopted constitutive law, the identified quantities may include tensile strength, fracture energy, residual tensile strength, or the control points of bilinear and multilinear softening laws [29–32]. These approaches can reproduce the response of a given composite effectively. However, the concrete matrix and fiber contribution are generally condensed into a single equivalent stress–crack opening relationship. The identified law is consequently associated with the fiber dosage, fiber distribution, bond conditions, and specimen configuration used during calibration. When the fiber volume fraction or reinforcement layout changes, the equivalent relationship must also change.

This limitation becomes more significant for HRC beams. A single measured load–deflection curve may include contributions from matrix fracture, fiber pull-out, bar yielding, bond interaction and compression-side damage. If all these mechanisms are represented by one equivalent constitutive relationship, the numerical response may reproduce the experiment without uniquely identifying the physical contribution of each constituent. Different combinations of assumed matrix, fiber, and steel properties may produce similar global curves, leading to non-unique solutions and limiting the transferability of the identified parameters to other reinforcement configurations.

The Bridged Crack Model provides an alternative framework, in which matrix and reinforcing phases retain their individual mechanical identities. The original model developed for RC beams described crack propagation through the fracture resistance of the concrete matrix and the closing forces supplied by the longitudinal reinforcement [28–30]. It was subsequently extended to brittle-matrix composites containing multiple discrete reinforcements and continuous or discontinuous fiber distributions [30–33]. Further developments put into evidence local instabilities, cyclic effects, and nonlinear structural behaviour [34]. Unlike homogenized cohesive models, these formulations explicitly relate crack propagation to the bridging forces generated by the reinforcing components.

The *Updated Bridged Crack Model* (UBCM) extends this framework by introducing softening fiber-slippage laws capable of reproducing the progressive fiber pull-out much better than the previous perfectly plastic law. Applications to FRC beams have demonstrated that the model can describe different post-cracking regimes and their dependence on fiber content, pull-out capacity, and structural size [34–39]. The formulation has subsequently been extended to HRC beams by representing concrete matrix, short fibers, and longitudinal steel bars as separate interacting phases [36]. Accordingly, the UBCM provides a physically based framework for distinguishing the loss of matrix resistance from the crack-closing actions supplied by fiber pull-out and steel reinforcement.

Previous UBCM investigations have mainly focused on the prediction of post-cracking regimes, minimum reinforcement conditions, and scale effects in FRC and HRC beams [32–36]. The model has also been combined with multi-objective inverse analysis to identify matrix and fiber-related properties from flexural responses [35]. However, a systematic identification methodology capable of separating matrix, fiber, and steel contributions within the complex failure behaviour of HRC beams has not yet been fully

established. In particular, the transferability of constituent properties identified from mechanically simpler specimens to HRC beams containing both reinforcing phases requires a dedicated validation.

The present study therefore develops a staged inverse-analysis methodology based on the UBCM for identifying the material parameters governing the flexural fracture response of HRC beams. Plain-concrete specimens are first used to identify the effective matrix stiffness and fracture toughness. FRC specimens without longitudinal reinforcement are then employed to determine the parameters governing fiber bridging and progressive pull-out, whereas RC specimens without fibers are used to identify the steel-bar yielding behaviour. The identified constituent properties are subsequently combined, without further adjustment, to predict the experimental responses of nine HRC configurations containing different fiber volume fractions and longitudinal reinforcement ratios.

The principal objective of the paper is to demonstrate that, despite the complex and interacting failure mechanisms illustrated in Figure 1, the global response of HRC beams can be decomposed into physically significant constituent properties through a mechanism-based inverse-analysis procedure. The proposed approach differs from conventional inverse methods based on a single equivalent constitutive law by isolating the material phases during calibration and assessing the single parameters through elementary failure mechanisms.

## 2. Updated Bridged Crack Model (UBCM)

The Updated Bridged Crack Model (UBCM) interprets hybrid-reinforced concrete as a multiphase system in which concrete matrix, longitudinal steel bars, and discontinuous fibres retain their individual mechanical roles. The matrix controls the initiation and advancement of the dominant crack, whereas the reinforcing phases oppose crack opening through distinct bridging mechanisms: stress mobilisation and yielding in the longitudinal bars, and progressive debonding and pull-out in the short fibres. This separation is particularly important for inverse analysis because it avoids representing the entire HRC response through a single equivalent constitutive relationship [34–36].

Figure 2 illustrates the conventional description of fibre-reinforced concrete through a resultant stress–crack opening law. The tensile-transfer capacity of the composite is obtained by combining the cohesive resistance of the concrete matrix with the bridging stress supplied by the fibres. At relatively small crack openings, the concrete matrix provides the principal resistance. As the crack develops, the matrix contribution progressively decreases, while an increasing proportion of the tensile transfer is sustained by the fibres intersecting the fracture plane. After the matrix resistance has been exhausted, the remaining response is governed mainly by fibre pull-out until the fibres cease to bridge the crack.

Although the resultant curve in Figure 2 can reproduce the global tensile behaviour of a particular FRC mixture, it does not preserve the separate contributions of the matrix and fibres. Moreover, the resultant law depends on the fibre dosage, orientation, distribution, and bond conditions associated with the specific material under investigation. The UBCM overcomes this limitation by introducing the matrix fracture resistance and the reinforcement bridging actions independently within the sectional equilibrium. In this way, changes in fibre or bar reinforcement can be represented through the corresponding reinforcing phase without redefining the complete constitutive response of the matrix-composite.

Figure 3 presents the critical cross-section considered in the UBCM. The section is rectangular, with thickness $b$, depth $h$, and initial crack or notch depth $a_0$, and is subjected to an external bending moment $M$. Damage is assumed to localise within this section, whereas the remaining portions of the beam are treated as predominantly elastic.

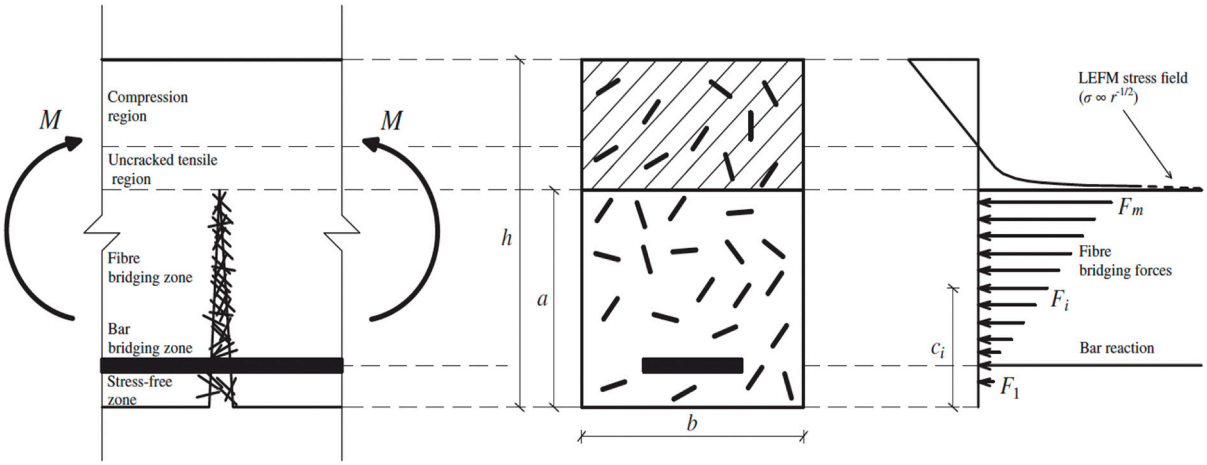



**Figure 3.** Critical cross-section in a hybrid reinforced concrete beam and stress distribution predicted by the Updated Bridged Crack Model (UBCM).

During crack propagation, four mechanically distinguishable regions can be recognised. The upper part of the section remains under compression. Below it, an uncracked tensile ligament continues to transmit elastic stresses. The open portion of the section contains a reinforcement-bridging zone, where longitudinal bars and short fibres connect the opposite crack faces. Finally, a stress-free region may develop near the tensile edge when the local opening becomes sufficiently large for the fibre action to be fully exhausted.

The reinforcing elements crossing the critical cross-section are represented through discrete layers located at different distances $c_i$ from the beam intrados. The total reinforcement consists of the prescribed longitudinal bar layers, $n_\mathrm{b}$, and the fibres intersecting the critical section, $n_\mathrm{f}$, $(n = n_\mathrm{b} + n_\mathrm{f})$. While $n_\mathrm{b}$ follows directly from the bar arrangement, $n_\mathrm{f}$ depends on fibre volume fraction and spatial distribution and is calculated as

$$n_\mathrm{f} = \alpha V_\mathrm{f} \frac{bh}{A_\mathrm{f}} \tag{1}$$

where $V_\mathrm{f}$ is the fibre volume fraction, $A_\mathrm{f}$ is the cross-sectional area of an individual fibre, and $\alpha$ is the fibre-orientation factor. The coefficient $\alpha$ accounts for the difference between the theoretical number of fibres associated with the prescribed volume fraction and the effective number crossing the fracture plane. It may be evaluated from the fractured surface or estimated through a statistical representation of fibre orientation and distribution [36].

At a given crack depth, only a portion of the reinforcing elements remains mechanically active. Fibres positioned ahead of the crack tip have not yet been intercepted, whereas fibres located in regions where pull-out has already been completed no longer transmit force. The number of active reinforcement layers, $m$, therefore changes continuously as the crack propagates.

The concrete matrix is treated as a linear-elastic phase. Accordingly, the crack-tip field is characterised by the mode-I stress-intensity factor $K_\mathrm{I}$. The applied moment tends to open the crack, whereas the forces transmitted by the active bars and fibres shield the crack tip and oppose its propagation. The combined stress-intensity factor is expressed as

$$K_\mathrm{I} = K_\mathrm{IM} - \sum_{i=1}^{m} K_{\mathrm{I}i} = \frac{M}{bh^{3/2}} Y_\mathrm{M} - \frac{\{Y_\mathrm{F}\}^\mathrm{T}\{F\}}{bh^{1/2}} \tag{2}$$

where $K_{IM}$ is the SIF contribution produced by the applied moment and $K_{\mathrm{I}i}$ is the SIF contribution associated with the $i$-th reinforcement force. In Equation (2), $Y_\mathrm{M}$ is the dimensionless shape function corresponding to the applied moment, $\{Y_\mathrm{F}\}$ is the vector of the

shape functions associated with the active bridging forces, and $\{F\}$ contains the corresponding fibre and bar forces. Crack propagation occurs when $K_{\mathrm{I}}$ reaches the matrix fracture toughness $K_{\mathrm{IC}}$.

The closing force generated by each active reinforcement depends on the crack opening at its position. The constitutive relationships of the reinforcing phases can be written in the general form

$$\sigma_i = f(w_i) \tag{3}$$

where $\sigma_i$ is the bridging stress in the $i$-th active reinforcement and $w_i$ is the corresponding crack-opening displacement. The function $f(w_i)$ is different for the longitudinal bars and short fibres because the two reinforcements resist crack opening through different mechanisms.

The longitudinal bars transfer tensile forces across the crack through the steel–concrete bond. As the crack opens, the bar stress is progressively mobilised over the transfer length until yielding occurs. This response is described through the hardening–perfectly plastic relationship shown in Figure 4:

$$\sigma_i(w_i) = \sigma_{\mathrm{y}}\left(\frac{w_i}{w_{\mathrm{y}}}\right)^{1/2}, \quad 0 < w_i \le w_{\mathrm{y}} \tag{4a}$$

$$\sigma_i(w_i) = \sigma_{\mathrm{y}}, \qquad w_i \ge w_{\mathrm{y}} \tag{4b}$$

where $\sigma_{\mathrm{y}}$ is the yield strength of the longitudinal reinforcement and $w_{\mathrm{y}}$ is the crack opening corresponding to the onset of yielding. Before $w_{\mathrm{y}}$, the bar stress increases progressively because the tensile force is transferred from the crack plane to the surrounding concrete through bond. Beyond this opening, the bar continues to bridge the crack at the yield stress.

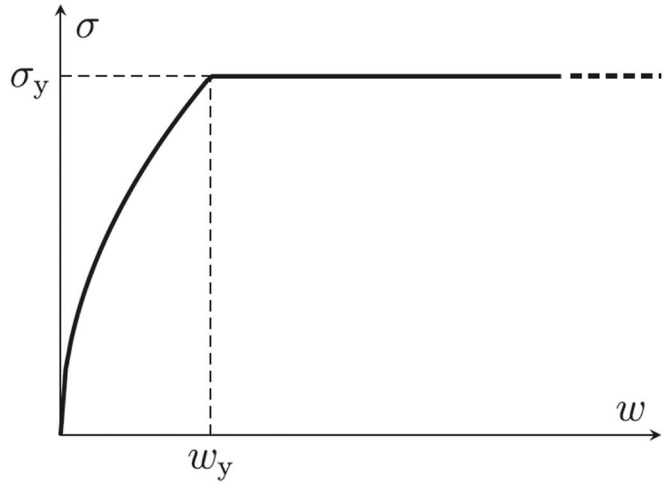



**Figure 4.** Steel-bar hardening-perfectly plastic constitutive law.

The crack opening corresponding to steel yielding is evaluated as

$$w_{\mathrm{y}} = \frac{\sigma_{\mathrm{y}}^2 \Phi}{4 E_{\mathrm{s}} \tau_{\mathrm{m}}} \tag{5}$$

where $\Phi$ is the bar diameter, $E_{\mathrm{s}}$ is the Young's modulus of the reinforcing steel, and $\tau_{\mathrm{m}}$ is the average shear stress transferred along the steel–concrete interface. Thus, the opening required to mobilise bar yielding depends not only on the steel strength but also on the bar geometry, elastic stiffness and bond-transfer conditions. The adopted relationship describes bar stress mobilisation and yielding but does not contain a terminal rupture criterion. Consequently, possible premature bar rupture in very lightly reinforced HRC

beams is recognised as an experimental failure mechanism but is not directly reproduced by the present constitutive law.

The response of a straight fibre, shown in Figure 5a, is governed mainly by debonding and frictional sliding. After the maximum slippage resistance has been mobilised, the available embedded length progressively decreases, causing a continuous reduction in the bridging stress. The fibre contribution disappears when the crack opening reaches the critical pull-out displacement $w_c$.

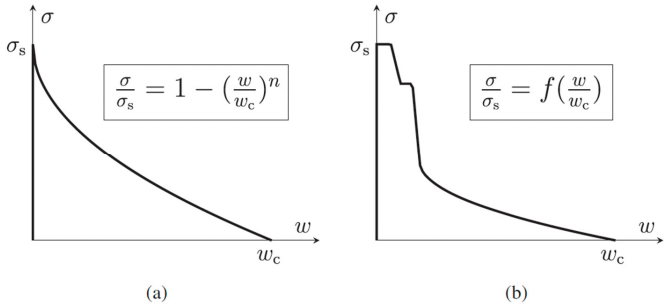



**Figure 5.** Steel-fibre rigid-softening constitutive laws: (**a**) straight fiber; (**b**) hooked-end fiber.

The hooked-end fibre response shown in Figure 5b is more complex because mechanical anchorage is added to the bond and frictional mechanisms. The hook initially resists extraction through local bending and straightening. This produces changes in the slope of the pull-out response before the fibre enters the final friction-controlled extraction stage. The constitutive shape therefore reflects the successive activation and degradation of bond, hook anchorage and sliding resistance [34–36].

In the UBCM, the fibres crossing the critical section are represented through an equivalent deterministic distribution, with their number determined by Equation (1), accounting for fibre volume fraction and orientation. The equivalent maximum pull-out force, ($F_s$), characterizes the peak bridging resistance of an active fibre, while ($w_c$) defines the crack opening at which its contribution vanishes. The adopted hooked-end fibre pull-out law follows the established UBCM formulation [34–36], with the collective bridging resistance depending on the number and pull-out state of the active fibres.

The crack openings and the bridging forces cannot be determined independently. The applied bending moment increases the opening of the critical section, whereas the forces transmitted by the active reinforcements reduce it. Their compatibility is expressed in matrix form as

$$\{w\} = \{\lambda_M\}M - [\lambda]\{F\} \quad (6)$$

where $\{w\}$ is the vector of crack-opening displacements at the active reinforcement levels, $\{\lambda_M\}$ is the vector of local compliances associated with the applied moment, and $[\lambda]$ is the matrix of local compliances associated with the bridging forces. The diagonal terms of $[\lambda]$ describe the effect of a reinforcement force on the opening at its own position, whereas the off-diagonal terms account for the interaction among forces acting at different levels of the crack. For a prescribed crack depth, the fracture moment, crack-opening profile and distribution of reinforcement forces are determined by simultaneously satisfying the crack-propagation condition in Equation (2), the reinforcement constitutive relationships in Equations (3)–(5), and the compatibility condition in Equation (6). Since the reinforcement forces depend on the crack openings, while the openings themselves depend on the forces, the solution is obtained iteratively.

Once the converged sectional state has been established, the local rotation is calculated as

$$\phi = \lambda_{MM} M - \{\lambda_M\}^T \{F\} \quad (7)$$

where $\lambda_{MM}$ is the rotational compliance associated with the external bending moment. The first term represents the rotation generated by the applied moment, while the second term represents the reduction in rotation resulting from the active crack-closing forces.

By repeating the solution for successive crack depths, the UBCM traces the evolution of the fracture moment and sectional rotation up to substantial separation of the critical section. The corresponding global load–deflection response is obtained by combining the localised rotation with the elastic deformation of the remaining beam and applying the equilibrium relationship of the four-point-bending configuration ($\delta = \delta_{elastic} + \delta_{crack}$). The resulting numerical response retains the separate roles of matrix cracking, steel-bar mobilisation and fibre pull-out and is therefore adopted as the forward model for the inverse-analysis procedure described in the following section.

## 3. Inverse-Analysis Identification

The inverse-analysis procedure is developed by exploiting the fact that different portions of the load–deflection response are governed predominantly by different fracture and reinforcement mechanisms. As discussed in relation to Figure 1, the measured response of an HRC beam may involve matrix cracking, fiber debonding, and pull-out, steel-bar mobilization and yielding, possible bar rupture and compression-side crushing. Identifying all associated properties simultaneously from a single HRC curve would lead to a strongly coupled problem, because different combinations of matrix, fiber, and steel parameters could generate similar global responses. The resulting solution could reproduce the experimental curve without providing a unique or physically meaningful description of the individual constituents.

To reduce this ambiguity, the present methodology separates the calibration into three stages. Plain-concrete specimens are first used to characterize the matrix response. FRC specimens without longitudinal bars are subsequently used to identify the fiber-related properties, and RC specimens without fibers are used to determine the yielding behaviour of the longitudinal reinforcement. The parameters obtained from these mechanically simpler configurations are finally combined in the UBCM to predict the response of HRC beams. The HRC specimens are therefore reserved for validation and are not involved in parameter calibration.

### *3.1. Identification of the Concrete-Matrix Response*

The initial branch $O - A$ in Figure 1 represents the response before propagation of the dominant flexural crack. During this stage, the global stiffness is controlled mainly by the concrete matrix and the specimen geometry. The crack-bridging actions of the fibers and longitudinal bars are not yet fully mobilised because a finite crack opening has not developed at the critical section. The initial response can therefore be interpreted without significant interference from fiber pull-out or steel yielding.

Within the UBCM, the slope of the pre-cracking branch is governed by the effective elastic modulus, $E^*$ (in cohesive state), whereas the load corresponding to Point $A$ is governed primarily by the Mode-I fracture toughness, $K_{IC}$. Increasing $E^*$ produces a steeper numerical response, while variation in $K_{IC}$ changes the load at which the crack begins to propagate. The two quantities affect different features of the curve and can therefore be identified by matching both the initial stiffness and the first-cracking condition.

A plain-concrete specimen is used for this stage because neither fiber bridging nor longitudinal reinforcement is present. Trial combinations of $E^*$ and $K_{IC}$ are introduced into

the UBCM, and the resulting numerical responses are compared with the experimental load–deflection envelope. The combination reproducing the ascending branch and the first-cracking load most satisfactorily is retained as the matrix-property estimate. The detailed calibration results are presented in Section 5.1.

### *3.2. Identification of the Fiber Pull-Out Response*

Once matrix cracking occurs, the tensile resistance supplied by the concrete decreases and the fibers crossing the fracture plane become mechanically active. The response between Points *A*, *B* and *C* in Figure 1 is therefore particularly informative for identifying the fiber-related properties. To isolate this contribution, the calibration is performed using FRC specimens without longitudinal steel bars.

The load recovery following Point *A* results from the progressive mobilization of the fibers intersecting the critical crack. The magnitude of this recovery is governed mainly by the equivalent fiber slippage strength, $\overline{\sigma_s} = \alpha\sigma_s$, which determines the maximum crack-bridging resistance that can be developed by the active fiber population. A larger value of $\sigma_s$ increases the post-cracking load sustained by the numerical specimen and modifies the level attained around Point *B*.

The subsequent reduction in load along branch $B - C$ reflects the progressive exhaustion of the fiber-bridging mechanism. At any stage of this response, the fibers crossing the critical section occupy different mechanical states: some are still strongly anchored, some are undergoing hook straightening and sliding, and others have already completed pull-out. The rate at which the collective bridging contribution disappears is governed primarily by the critical pull-out displacement, $w_c$. A larger $w_c$ allows the fibers to remain active over a greater crack opening and consequently extends the post-cracking branch and increases the energy absorbed before complete pull-out.

The effects of $\sigma_s$ and $w_c$ are related but not identical. The former primarily controls the post-cracking load level, whereas the latter strongly affects the extent and descending profile of the response. A parameter combination that reproduces the maximum load accurately may therefore provide an inadequate description of the overall post-cracking branch, while another combination may reproduce the curve area but underestimate the maximum resistance.

For this reason, the fiber parameters are identified through a multi-objective optimization procedure based on two complementary comparisons: the difference between the experimental and numerical maximum loads and the difference between the corresponding areas under the load–deflection curves. Each admissible pair $(\sigma_s|w_c)$ produces one numerical response and therefore one point in the objective-function plane. The nondominated solutions form the Pareto front, and the parameter pair giving the most balanced reduction in both discrepancies is selected as the best-fitting solution [35].

The search is restricted to physically meaningful values: the equivalent slippage strength must remain positive, and the critical pull-out displacement must be compatible with the available fiber embedment length. The detailed Pareto procedure and the identified results for the three FRC configurations are presented in Section 5.2. Using several fiber volume fractions provides an additional check on whether the identified properties remain reasonably consistent when the number of fibers crossing the critical section changes.

### *3.3. Identification of the Steel-Bar Yielding Response*

The contribution of the longitudinal reinforcement is identified from RC specimens without fibers. This selection eliminates the additional load transfer associated with fiber pull-out and enables the yielding-controlled portion of the response to be interpreted directly.

For a lightly reinforced concrete beam, matrix cracking is followed by mobilization of the bars across the dominant crack. With increasing deformation, the bar stress approaches the yield strength and the response develops towards the approximately plastic branch represented schematically by $A - D$ in Figure 1. At higher, but still moderate, reinforcement ratios, the load may continue increasing after first cracking before approaching the plateau represented by $E - F$. In either case, the load level maintained after yielding is strongly governed by the steel yield strength, $\sigma_y$.

The value of $\sigma_y$ is therefore identified by varying it within the UBCM until the numerical yielding branch reproduces the corresponding experimental response. The comparison is concentrated on the load level and general development of the plastic region rather than on the initial branch, which remains controlled primarily by the concrete matrix.

Three longitudinal reinforcement ratios are considered so that the identified steel property is not obtained from only one structural configuration. The selected range extends from very low to moderate reinforcement and is intended to capture the progressive transition from a lightly reinforced yielding response to a more pronounced plastic plateau. Highly reinforced beams are not used for calibration because compression-side crushing may become dominant before the bar-controlled response is fully developed. Under those conditions, additional compressive-fracture parameters would influence the global response and the yield strength could not be isolated reliably.

Possible bar rupture in very lightly reinforced HRC beams is also excluded from the identification process. Although such a mechanism may occur experimentally when fiber-enhanced bond promotes strong strain localization at the dominant crack, the steel constitutive law adopted in the present UBCM formulation describes bar mobilization and yielding but does not include a terminal rupture condition. The steel property is therefore identified exclusively from RC responses exhibiting a recognizable yielding-controlled branch.

It should be clarified that the matrix parameters are evaluated within the individual calibration configurations to account for variations in initial stiffness and first-cracking resistance. Subsequently, the average values of the identified constituent parameters are adopted as a common parameter set for predicting the HRC responses, without further adjustment.

## 4. Experimental Program

The experimental data used in the present study were obtained from the broader research programme Fracture Study on Next Generation Reinforced Concrete Structures, conducted at Shantou University. The current investigation considers only the beams having a depth of 200 mm and a thickness of 200 mm. All specimens were geometrically identical, with a span-to-depth ratio of 6 and an initial notch depth equal to 10% of the beam depth. The notch was introduced at the midspan tensile face to ensure localization of the dominant flexural crack within the constant-moment region. Sample preparation and testing guidelines are followed according to the Chinese standard GB/T 50081-2019 [40].

The characteristic compressive strength of concrete, as provided by the manufacturer, was 40 MPa. The longitudinal reinforcement consisted of HRB400 deformed steel bars with diameters of 8 and 12 mm. Hooked-end steel fibers having a length of 30 mm and a diameter of 0.5 mm were used as discontinuous reinforcement. The fiber volume fraction, $V_f$, was varied as 0.2%, 0.4%, and 0.8%, whereas the longitudinal reinforcement ratio, $\rho$, was varied as 0.13%, 0.28%, and 0.50%. The remaining material properties required in the UBCM were not prescribed independently because their identification constitutes the principal objective of the present inverse-analysis procedure.

The specimens were designated as HRC_X_Y_Z, where $X$ represents the beam depth in millimetres, $Y$ denotes the fiber volume fraction in percent, and $Z$ denotes the longitudinal reinforcement ratio in percent. For example, HRC_200_0.4_0.28 represents a beam with a

depth of 200 mm, a fiber volume fraction of 0.4%, and a longitudinal reinforcement ratio of 0.28%.

A total of 16 reinforcement configurations were considered, with three nominally identical specimens tested for each configuration. Accordingly, the experimental database consisted of 48 four-point-bending tests. Seven configurations were used for calibration, and remaining nine HRC configurations, obtained by combining fiber and longitudinal steel bar percentages, were reserved for validation. The complete specimen matrix is reported in Table 1.

**Table 1.** Specimen details.

| Specimen | Depth (mm) | Role | $V_f$ (%) | $\rho$ (%) |
|---|---|---|---|---|
| HRC_200_0.0_0.0 | 200 | Matrix calibration | 0.0 | 0.0 |
| HRC_200_0.2_0.0 | 200 | Fiber calibration | 0.2 | 0.0 |
| HRC_200_0.4_0.0 | 200 | Fiber calibration | 0.4 | 0.0 |
| HRC_200_0.8_0.0 | 200 | Fiber calibration | 0.8 | 0.0 |
| HRC_200_0.0_0.13 | 200 | Bar calibration | 0.0 | 0.13 |
| HRC_200_0.0_0.28 | 200 | Bar calibration | 0.0 | 0.28 |
| HRC_200_0.0_0.50 | 200 | Bar calibration | 0.0 | 0.50 |
| HRC_200_0.2_0.13 | 200 | HRC validation | 0.2 | 0.13 |
| HRC_200_0.2_0.28 | 200 | HRC validation | 0.2 | 0.28 |
| HRC_200_0.2_0.50 | 200 | HRC validation | 0.2 | 0.50 |
| HRC_200_0.4_0.13 | 200 | HRC validation | 0.4 | 0.13 |
| HRC_200_0.4_0.28 | 200 | HRC validation | 0.4 | 0.28 |
| HRC_200_0.4_0.50 | 200 | HRC validation | 0.4 | 0.50 |
| HRC_200_0.8_0.13 | 200 | HRC validation | 0.8 | 0.13 |
| HRC_200_0.8_0.28 | 200 | HRC validation | 0.8 | 0.28 |
| HRC_200_0.8_0.50 | 200 | HRC validation | 0.8 | 0.50 |

All specimens were produced by Guangdong Donghong Zhugong Technology using the same manufacturing and quality-control procedures and were subsequently transported to the Material Testing Laboratory of Shantou University. The beams were tested under four-point bending using the simply supported arrangement shown in Figure 6. Loading was applied under crack-mouth-opening-displacement control to capture both the pre-cracking and post-cracking responses. During testing, the applied load and corresponding displacement were continuously recorded to obtain the complete load–deflection curves used in the inverse-analysis procedure.

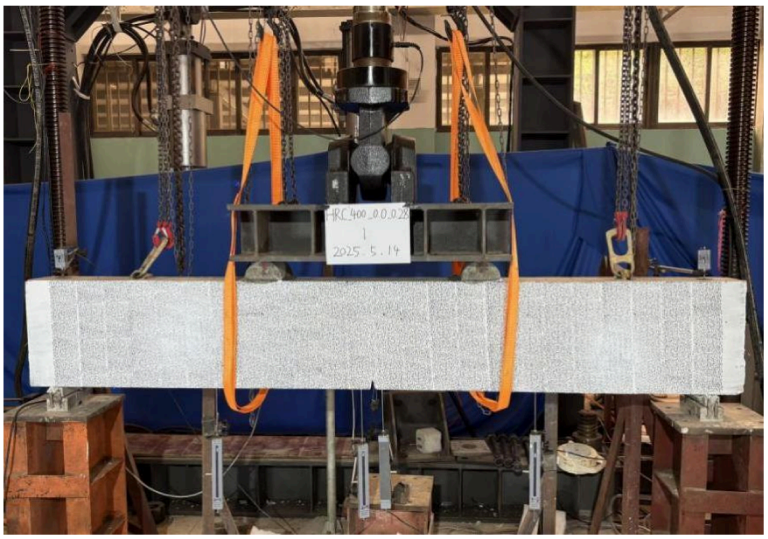


**Figure 6.** Testing setup.

The shaded experimental envelopes represent the common overlapping region of the load–deflection responses obtained from the three nominally identical specimens in each configuration.

## 5. Material Parameter Identification

### *5.1. Identification of $K_{IC}$ and E**

The fracture properties of the concrete matrix were identified using the plain-concrete specimen HRC_200_0.0_0.0, which contained neither fibers nor longitudinal steel reinforcements. The absence of reinforcing phases ensures that the measured load–deflection response is governed primarily by the stiffness and fracture toughness of the concrete matrix, thereby allowing $E^*$ and $K_{IC}$ to be identified without interference from fiber pull-out or steel-bar yielding.

According to the UBCM, the effective Young's modulus $E^*$ primarily controls the slope of the ascending branch, whereas the fracture toughness $K_{IC}$ governs the load level at which the dominant crack initiates and begins to propagate. Consequently, different combinations of $E^*$ and $K_{IC}$ were introduced into the model, and the corresponding numerical load–deflection curves were compared with the experimental response. The experimental results of the three nominally identical specimens are represented by the shaded region in Figure 7, while the solid line denotes the numerical prediction. The identified value of $E^*$ provides a satisfactory representation of the initial slope, while $K_{IC}$ reproduces the experimentally observed first-cracking load. The numerical curve also captures the abrupt reduction in load-carrying capacity following crack initiation, which is characteristic of the unstable fracture response of the unreinforced specimen.

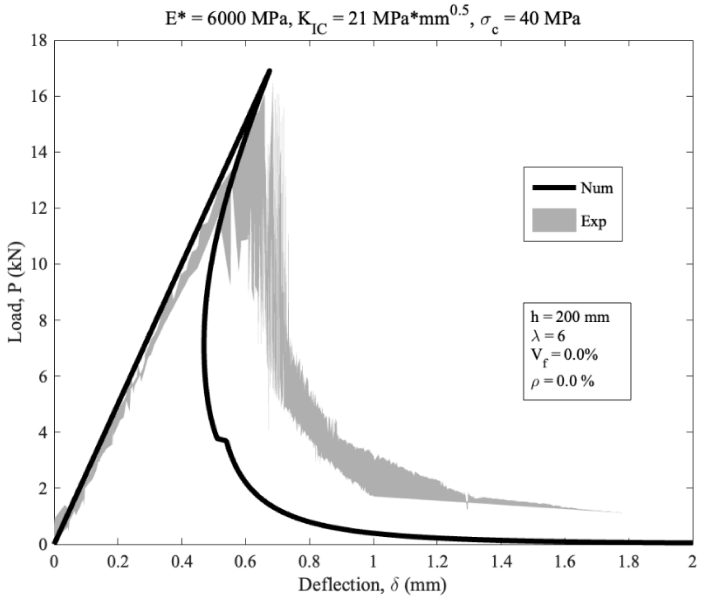



**Figure 7.** Numerical calibration of specimen HRC_200_0.0_0.0 to identify elastic modulus and fracture toughness of concrete.

A comparatively larger dispersion is observed in the experimental post-peak branch. This variation is expected because the descending response of plain concrete is highly sensitive to crack localization and a local material heterogeneity. Since the present calibration is intended primarily to identify the matrix stiffness and resistance to crack initiation, greater importance is assigned to the ascending branch and the first-cracking condition than to the complete post-peak tail. The identified values are subsequently used as the concrete-matrix parameters in the calibration of the fiber- and bar-reinforced specimens.

### *5.2. Identification of $F_s$ and $w_c$*

The parameters governing the fiber-bridging mechanism were identified from the FRC specimens HRC_200_0.2_0.0, HRC_200_0.4_0.0, and HRC_200_0.8_0.0, which contained fiber volume fractions of 0.2%, 0.4%, and 0.8%, respectively, without longitudinal steel reinforcement. The absence of reinforcing bars allows the post-cracking response to be associated predominantly with the progressive mobilization and pull-out of the hooked-end steel fibers.

For each specimen series, the matrix-related parameters $E^*$ and $K_{IC}$ were first selected to reproduce the initial effective stiffness and the first-cracking load. These parameters mainly affect the response up to the first kink of the load–deflection curve, before the fiber-bridging mechanism becomes dominant. Subsequently, the equivalent maximum fiber pull-out force, $F_s$, and the critical pull-out displacement, $w_c$, were varied to reproduce the post-cracking response. Here, $F_s$ controls the magnitude of the crack-closing force developed by the active fibers, whereas $w_c$ defines the crack opening at which the fibers are completely pulled out and their bridging action is exhausted.

The two fiber parameters affect different, although mutually dependent, characteristics of the load–deflection response. An increment in $F_s$ primarily increases the post-cracking load level and the maximum resistance attained after matrix cracking. On the contrary, an increment in $w_c$ extends the displacement range over which the fibers remain active and therefore modifies the descending branch and the total energy absorbed during pull-out. Consequently, a parameter pair providing an accurate prediction of the maximum load does not necessarily reproduce the complete post-cracking branch.

A multi-objective optimization procedure based on the Pareto approach was therefore adopted [35]. As illustrated in Figure 8a, the numerical and experimental responses were compared in terms of two quantities: the difference in maximum load, $\Delta P_{max}$ (kN), and the difference in the area under the load–deflection curve, $\Delta A$ (kN · mm). The first objective evaluates the prediction of the load-bearing capacity, whereas the second provides a global measure of the agreement over the complete response, including the pull-out branch.

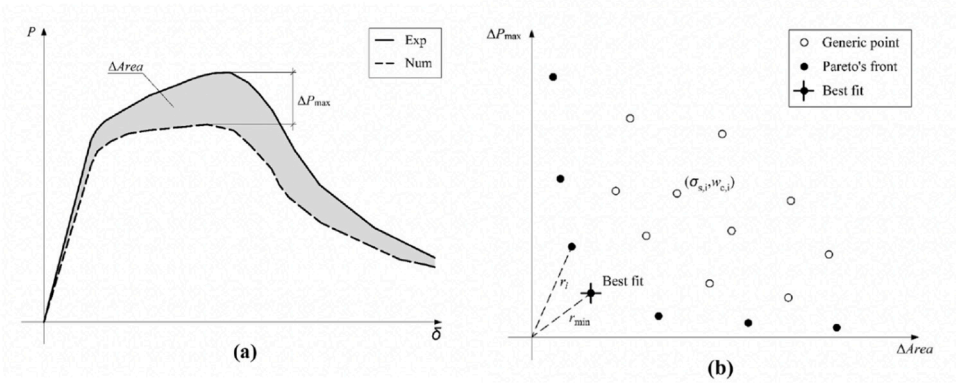



**Figure 8.** Pareto's procedure: (**a**) representation of $\Delta P_{max}$ and (**b**) associated $\Delta Area$ multi- objective optimization.

The two objective functions were selected to represent complementary characteristics of the experimental response, namely the maximum load and the integrated area under the load–deflection curve. The resulting Pareto solutions were evaluated to identify a compromise between load-carrying resistance and overall deformation work. Although these objectives characterize the principal features of the flexural response, they do not independently quantify every local difference in curve shape, which remains a limitation of the adopted identification criterion.

For each trial pair ($F_s|w_c$), the UBCM analysis produces one numerical load–deflection curve and the corresponding values of $\Delta P_{max}$ and $\Delta A$. Each trial solution can therefore be represented by a point in the objective-function plane shown in Figure 8b. The non-dominated solutions constitute the Pareto front, for which improvement in one objective cannot be achieved without worsening the other. Among these solutions, the parameter pair having the minimum distance from the origin was selected as the best compromise between the two objective functions. The search was restricted to positive values of $F_s$, while $w_c$ was limited between zero and one-half of the fiber length, in accordance with the physical range of fiber embedment [37].

As shown in Figure 9a, the response of the specimen with $V_f = 0.2\%$ remains relatively close to that of plain concrete. The limited number of fibers crossing the critical section is insufficient to produce a pronounced post-cracking recovery. The response is therefore characterized by a sharp loading reduction and drop after the first cracking, if the snap-back branch is not adequately controlled, which is followed by a lower residual softening branch. The numerical prediction reproduces the first-cracking load and the catastrophic nature of the response.

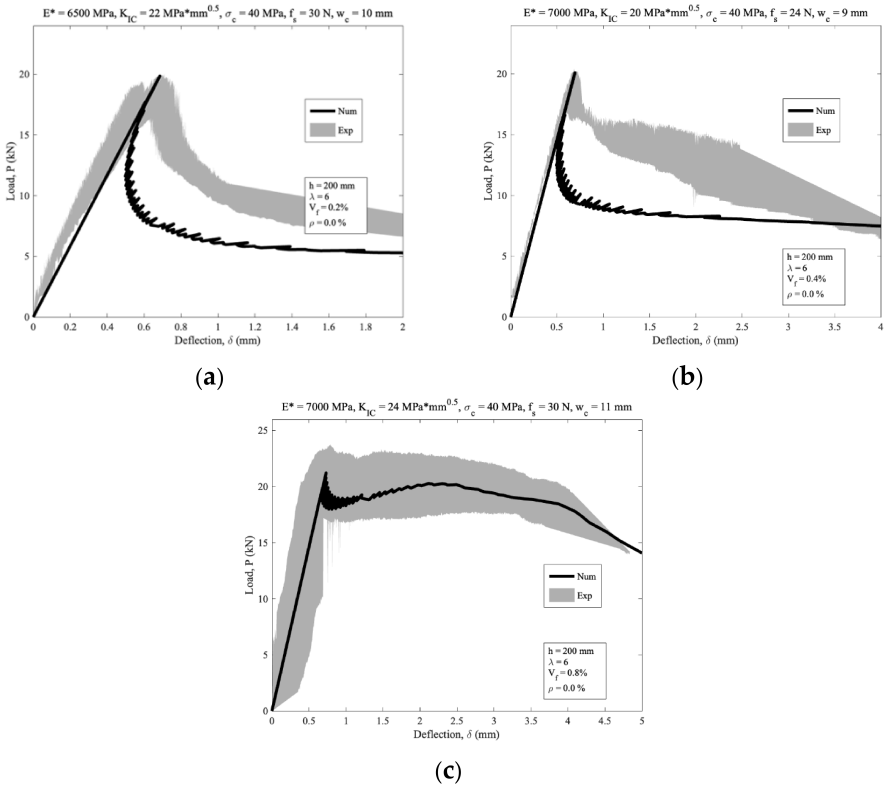



**Figure 9.** Numerical calibration of specimens: (**a**) HRC_200_0.2_0.0; (**b**) HRC_200_0.4_0.0; (**c**) HRC_200_0.8_0.0.

Increasing the fiber volume fraction to 0.4% produces a more evident residual load-carrying capacity after matrix cracking, as shown in Figure 9b. The UBCM captures the first-cracking condition and the subsequent transition towards the fiber-controlled branch. Nevertheless, some discrepancy remains in the intermediate post-cracking region, where the experimental specimens exhibit considerable variability. This scatter reflects the random number, position, and orientation of the fibers intersecting the localized fracture plane.

At the highest fiber content, a substantial improvement in the post-cracking response is observed. Following the first kink, the load is sustained over a considerably larger displacement range, producing a broad post-cracking branch before the final pull-out-

controlled decay. As shown in Figure 9c, the numerical curve reproduces the principal load level, the extended fiber-bridging stage, and the eventual reduction in resistance. Local fluctuations in the numerical response arise from the discrete activation and pull-out of the fibers represented within the UBCM.

The three independently identified values of $F_s$ range from 24 to 30 N, while $w_c$ varies between 9 and 11 mm. The relatively limited variation indicates that the identified quantities are associated primarily with the common fiber type and fiber–matrix interaction rather than with the fiber volume fraction itself. The influence of $V_f$ is introduced separately in the UBCM through the number of fibers crossing the critical section. Accordingly, increasing the fiber content modifies the global flexural response without requiring a fundamentally different pull-out law for each mixture.

### *5.3. Identification of $\sigma_y$*

The yield strength of the longitudinal reinforcement was identified from the RC specimens HRC_200_0.0_0.13, HRC_200_0.0_0.28, and HRC_200_0.0_0.50, containing longitudinal reinforcement ratios of 0.13%, 0.28%, and 0.50%, respectively, without steel fibers. The absence of fibers isolates the crack-bridging contribution of the longitudinal bars and avoids any interference from fiber pull-out during the identification of $\sigma_y$.

For each specimen series, $E^*$ and $K_{IC}$ were first selected to reproduce the initial slope and first-cracking condition. After matrix cracking, the longitudinal bars progressively mobilize their tensile resistance through bond transfer with the surrounding concrete. As the crack opening increases, the bar stress approaches the yield strength and the load–deflection response develops towards a yielding-controlled branch. According to the UBCM, the load level sustained during this stage is governed predominantly by $\sigma_y$. Therefore, the steel yield strength was varied until the numerical post-cracking response provided the closest agreement with the experimental results.

Three reinforcement ratios were considered to examine whether a common steel parameter could reproduce the responses from very lightly to moderately reinforced beams. More highly reinforced specimens were not included in the calibration because compression-side crushing may become significant before a clearly distinguishable bar-controlled response develops. Under such conditions, the measured curve would depend not only on steel yielding but also on the compression damage and crushing energy of concrete.

The calibration results are presented in Figure 10. For all three RC configurations, the experimental responses of the nominally identical specimens are shown by the shaded regions, while the solid curves represent the corresponding UBCM predictions.

For specimen HRC_200_0.0_0.13, shown in Figure 10a, the very low reinforcement ratio results in a pronounced reduction in load immediately after matrix cracking. The small reinforcement area is initially unable to compensate fully for the sudden loss of tensile resistance in the concrete, and the response subsequently recovers as the bar force is progressively mobilized. The numerical curve captures this characteristic transition from unstable matrix cracking to a bar-controlled response. A comparatively large scatter is observed among the experimental curves, particularly in the post-cracking region, because the response of such lightly reinforced beams is highly sensitive to crack localization, bond conditions, and the development of steel strain near the dominant crack.

When the reinforcement ratio is increased to 0.28%, the post-cracking reduction becomes substantially smaller and the response develops towards a more distinct yielding plateau. As shown in Figure 10b, the numerical prediction reproduces both the rapid mobilization of the longitudinal reinforcement after cracking and the load level maintained during the subsequent yielding-controlled stage. The improved agreement relative to the

0.13% series indicates that the steel contribution can be identified more clearly when the bar reinforcement is sufficient to stabilize crack propagation.

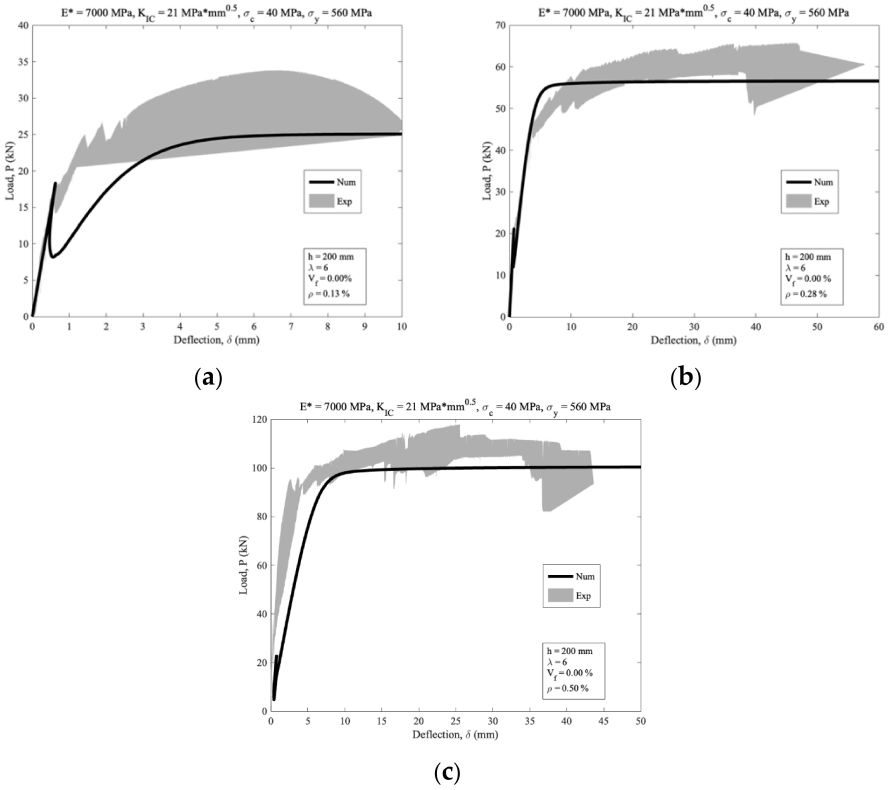



**Figure 10.** Numerical calibration of specimens: (**a**) HRC_200_0.0_0.13; (**b**) HRC_200_0.0_0.28; (**c**) HRC_200_0.0_0.50.

For specimen HRC_200_0.0_0.50, shown in Figure 10c, the larger reinforcement area produces a continued increment in load after first cracking, followed by a well-defined plateau. In this case, the response is predominantly governed by the longitudinal bars, and the influence of the initial matrix instability becomes comparatively limited. The UBCM prediction reproduces the principal load level and the development of the yielding branch using the same value of $\sigma_y$ identified for the two lower reinforcement ratios.

The consistent value of $\sigma_y = 560$ MPa obtained for all three RC configurations indicates that the identified parameter is associated with the mechanical behaviour of the reinforcing steel rather than with the reinforcement ratio. Changes in $\rho$ are represented separately in the UBCM through the reinforcement area and therefore alter the global load-carrying capacity without requiring a different yield strength for each specimen series. The agreement achieved over the three reinforcement levels supports the use of the identified value in the subsequent simulations of HRC beams containing both longitudinal bars and discontinuous fibers. The identified value of 560 MPa represents an effective yielding parameter within the adopted UBCM constitutive relationship. Although the reinforcement is classified as HRB400, the identified parameter should not be interpreted as an independently measured tensile yield strength of the steel bars.

## 6. Prediction of the HRC Beam Flexural Behaviour and Validation

The material parameters identified from the seven calibration configurations are summarized in Table 2. The average values obtained from the independent plain-concrete, FRC, and RC analyses are: $K_{IC} = 21.43$ MPa$\sqrt{\text{mm}}$, $E^* = 6785.71$ MPa, $F_s = 28$ N, $w_c = 10$ mm, and $\sigma_y = 560$ MPa. The relatively limited variation among the identified values indicates that

the parameters primarily characterize concrete matrix, fiber–matrix pull-out response, and reinforcing steel bars, globally, rather than any particular reinforcement configuration.

**Table 2.** Identified material properties.

| Specimen | $K_{IC}$ (MPa mm$^{0.5}$) | $E^*$ (MPa) | $f_s$ (N) | $w_c$ (mm) | $\sigma_y$ (MPa) |
|---|---|---|---|---|---|
| HRC_200_0.0_0.0 | 21 | 6000 | - | - | - |
| HRC_200_0.2_0.0 | 22 | 6500 | 30 | 10 | - |
| HRC_200_0.4_0.0 | 20 | 7000 | 24 | 9 | - |
| HRC_200_0.8_0.0 | 24 | 7000 | 30 | 11 | - |
| HRC_200_0.0_0.13 | 21 | 7000 | - | - | 560 |
| HRC_200_0.0_0.28 | 21 | 7000 | - | - | 560 |
| HRC_200_0.0_0.50 | 21 | 7000 | - | - | 560 |
| Average value | 21.43 | 6785.71 | 28 | 10 | 560 |
| Standard deviation | 1.27 | 393.39 | 3.46 | 1 | 0.0 |
| CV (%) | 5.93 | 5.79 | 12.37 | 10 | 0.0 |

It should be emphasized that the parameters summarized in Table 2 are obtained through inverse identification of the structural load–deflection responses. They therefore represent effective parameters within the adopted UBCM formulation rather than independently measured constituent properties. Their identification may also be influenced by aspects of the experimental response and modelling idealizations not explicitly resolved in the sectional formulation.

The parameters were identified for each calibration configuration using the corresponding experimental responses. Therefore, the reported statistical values describe variations among the identified configuration-level parameters rather than individual specimen-level material variability.

To evaluate their transferability, these average parameters were introduced into the UBCM to predict the responses of the nine HRC configurations. No parameter was readjusted using the HRC experimental curves. Consequently, the comparisons presented in Figures 11–13 represent a genuine validation of both the identified material parameters and the predictive capability of the UBCM. In each figure, the shaded region represents the experimental range obtained from the three nominally identical specimens, whereas the solid line represents the numerical prediction.

Figure 11 presents the results for $V_f = 0.2\%$ and longitudinal reinforcement ratios of 0.13%, 0.28%, and 0.50%. Despite the relatively low fiber content, the UBCM reproduces the progressive change from a fracture-sensitive response at the lowest bar ratio to a stable, steel-controlled response at the higher reinforcement levels. The numerical curves capture initial slope, first-cracking load, and average post-cracking load level. Some underestimation is observed in the lightly reinforced case, where the response is particularly sensitive to the small number and random orientation of fibers intersecting the critical section.

The comparisons for $V_f = 0.4\%$ are shown in Figure 12. The increased fiber content produces a more evident post-cracking contribution, particularly for the beams with low and intermediate longitudinal reinforcement. The UBCM successfully reproduces the recovery of load after matrix cracking and the subsequent transition towards a stable reinforcement-controlled response. At $\rho = 0.50\%$, the numerical prediction closely follows the experimental plateau, demonstrating that the steel-bar behaviour identified from the RC specimens remains applicable in the presence of fibers.

Figure 13 presents the validation results for $V_f = 0.8\%$. At this fiber content, the experimental responses exhibit substantial post-cracking resistance over all three longitudinal reinforcement ratios. The numerical curves reproduce the maximum load, the broad post-cracking response, and the gradual transition from fiber-dominated behaviour at low $\rho$ to steel-dominated behaviour at larger $\rho$. Minor differences occur around the local

maximum and descending branch, but the predictions remain generally consistent with the experimental output.

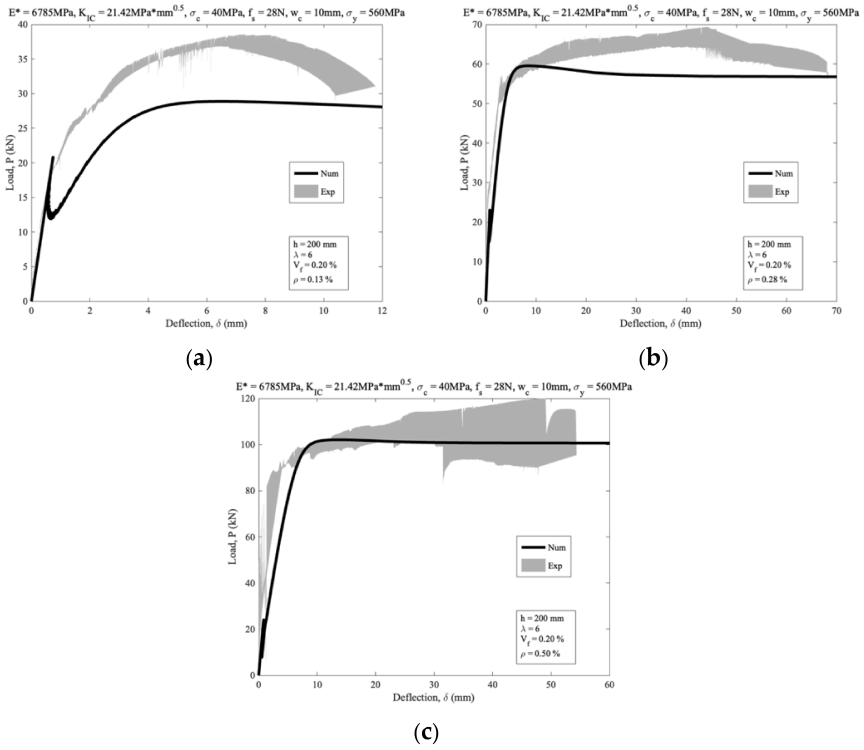



**Figure 11.** Comparison between experimental results and their numerical predictions for: (**a**) HRC_200_0.2_0.13; (**b**) HRC_200_0.2_0.28; (**c**) HRC_200_0.2_0.50.

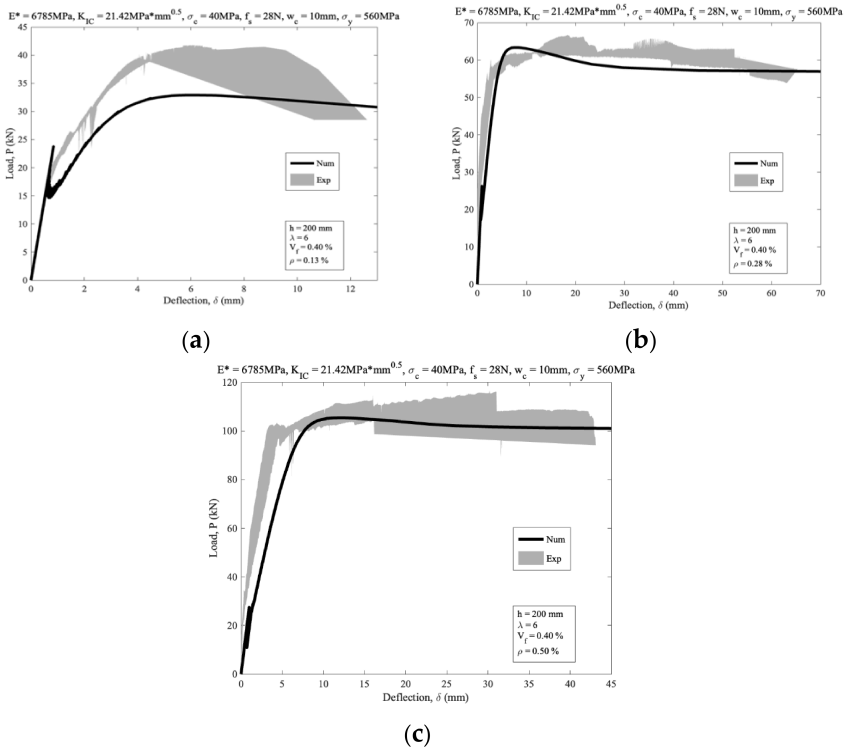



**Figure 12.** Comparison between experimental results and their numerical predictions for: (**a**) HRC_200_0.4_0.13; (**b**) HRC_200_0.4_0.28; (**c**) HRC_200_0.4_0.50.

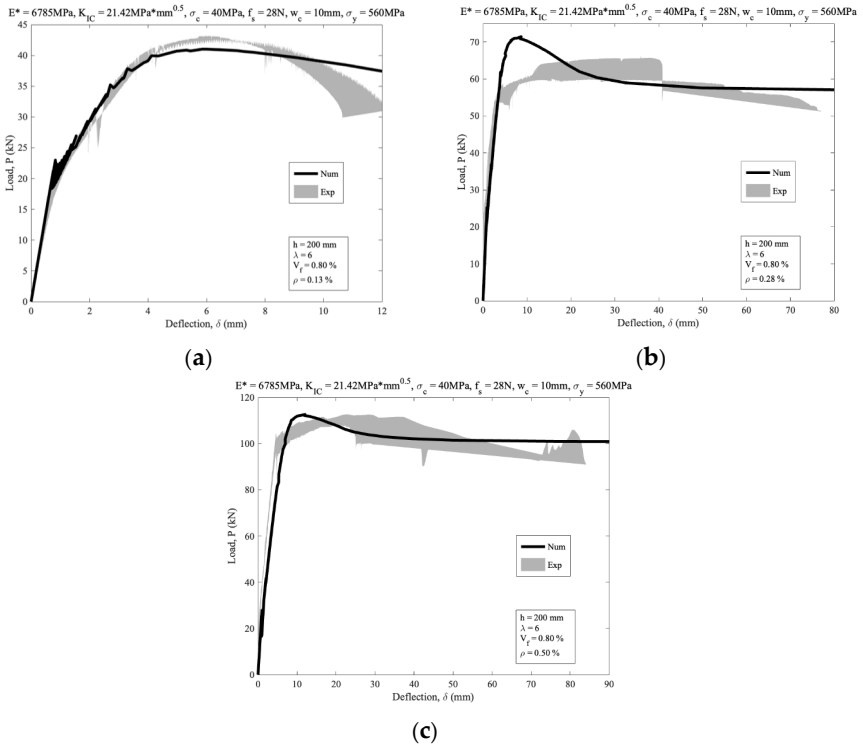



**Figure 13.** Comparison between experimental results and their numerical predictions for: (**a**) HRC_200_0.8_0.13; (**b**) HRC_200_0.8_0.28; (**c**) HRC_200_0.8_0.50.

Overall, the UBCM correctly predicts the systematic influence of both reinforcing phases. For a constant fiber volume fraction, increasing the longitudinal reinforcement ratio raises the load-carrying capacity and progressively transforms the response into a stable yielding-controlled plateau. Conversely, for a constant reinforcement ratio, increasing the fiber volume fraction improves the resistance following matrix cracking and extends the deformation range over which stresses can be transferred across the crack. These experimentally observed transitions are reproduced using a single set of average material parameters.

The largest deviations are found in configurations with low longitudinal reinforcement and low-to-moderate fiber contents. In these cases, the response is drastically affected by local crack formation and by the actual number, orientation, and anchorage of fibers crossing the fracture plane. The UBCM represents these inherently random effects through an equivalent deterministic fiber distribution and therefore cannot reproduce every local fluctuation observed experimentally. Nevertheless, the model consistently captures stiffness, cracking load, post-cracking resistance, and deformation trend across the complete validation matrix.

The validation confirms the efficiency of the proposed inverse-analysis procedure. Material parameters identified separately from plain-concrete, FRC, and RC specimens can be combined directly to predict the flexural behaviour of HRC beams without further calibrations. More importantly, the UBCM is able to reproduce the complex transition among matrix cracking, fiber pull-out, and steel-bar yielding, while maintaining the individual mechanical contribution of each constituent. The model therefore provides not only satisfactory agreement with the experimental responses but also a physically meaningful framework for identifying and transferring material parameters among different hybrid-reinforcement configurations.

The present validation demonstrates the transferability of the identified effective parameters across different combinations of fibre volume fraction and longitudinal reinforcement ratio within the investigated beam geometry and material system. Further validation across

different structural sizes, concrete mixtures, and fibre types is required to establish their broader applicability.

## 7. Discussion and Conclusions

The present study develops a UBCM-based inverse-analysis procedure for identifying the constituent properties governing the flexural response of hybrid-reinforced concrete beams. The main difficulty arises from the simultaneous or sequential activation of matrix cracking, fiber pull-out, and steel-bar yielding within a single load–deflection response. The UBCM is well suited to this problem because it preserves these mechanisms as separate contributions rather than combining them into a single equivalent constitutive law.

For clarity, the identification was performed in stages. Plain-concrete specimens were used to identify $E^*$ and $K_{IC}$, FRC specimens were used to determine, focusing on $F_s$ and $w_c$, and RC specimens were used to identify $\sigma_y$, specifically. This separation was adopted mainly to demonstrate the sensitivity of the structural response to each parameter and to verify their physical interpretation. The reasonably consistent values obtained from different calibration specimens indicate that the identified quantities represent constituent-level properties rather than parameters tied to one particular reinforcement configuration.

Although the staged procedure reduces parameter coupling and provides reasonably consistent identified values, it does not establish the strict mathematical uniqueness of the inverse solution. In particular, uncertainty in the matrix parameters may influence the subsequently identified reinforcement parameters, especially at low fibre contents where the response remains strongly governed by matrix cracking. A detailed assessment of parameter correlations and uncertainty propagation therefore remains an important direction for future investigation.

The identified average properties were subsequently used to predict the flexural behaviour of nine HRC configurations without further calibrations. The UBCM reproduced the main changes caused by varying the fiber volume fraction and longitudinal reinforcement ratio, including the transition from matrix-controlled fracture to fiber-supported post-cracking resistance and finally to steel-controlled yielding. The agreement with the experimental response confirms both the transferability of the identified parameters and the capability of the UBCM to represent the interaction between the two reinforcing phases.

The remaining deviations are mainly associated with the random number, orientation, and anchorage of fibers crossing the critical crack, particularly in lightly reinforced specimens. These effects are represented in the UBCM through an equivalent deterministic fiber distribution and therefore cannot reproduce all specimen-to-specimen fluctuations. Nevertheless, the model captures cracking load, post-cracking resistance, and deformation trends across the complete validation matrix.

An important outcome of this study is that the staged identification procedure is not a compulsory requirement. It was adopted to provide a transparent interpretation of the individual mechanisms and to illustrate the sensitivity of the response to each parameter. Since the UBCM already includes matrix fracture, fiber pull-out, and steel yielding within the same formulation, $E^*$, $K_{IC}$, $F_s$, $w_c$, and $\sigma_y$ may also be identified simultaneously from an HRC load–deflection response through a multi-parameter optimisation procedure.

Consequently, separate plain-concrete, FRC, and RC beams do not necessarily need to be cast solely for parameter identification. A sufficiently informative HRC response can be used directly, provided that appropriate parameter bounds and objective functions are adopted. The staged procedure presented here should therefore be regarded as a means of demonstrating identifiability and parameter sensitivity, rather than as a restriction of the inverse-analysis framework.

The principal conclusions are:

1. The UBCM enables matrix, fiber, and steel contributions to be identified separately within the complex flexural response of HRC beams.
2. The staged inverse analysis provides a clear physical interpretation of the influence of $E^*$, $K_{IC}$, $F_s$, $w_c$, and $\sigma_y$.
3. The identified average parameters successfully predicted nine different HRC configurations without recalibration, confirming their transferability.
4. The UBCM effectively reproduces the transition among matrix cracking, fiber pull-out, and steel-bar yielding.

**Author Contributions:** Conceptualization, B.K. and A.C.; methodology, B.K., D.X. and A.C.; software, B.K.; validation, B.K.; formal analysis, B.K.; investigation, B.K. and D.X.; data curation, B.K. and D.X.; writing—original draft preparation, B.K.; writing—review and editing, B.K. and A.C.; visualization, A.C.; supervision, A.C.; project administration, A.C. and D.X.; funding acquisition, A.C. All authors have read and agreed to the published version of the manuscript.

**Funding:** This research was funded by the Chang Jiang Chair Professorship, grant number NTF23025.

**Data Availability Statement:** Some or all data, models, or code that support the findings of this study are available from the corresponding author upon reasonable request.

**Conflicts of Interest:** The authors declare no conflicts of interest.

## Nomenclature

| Symbol | Definition | Unit |
|---|---|---|
| A | Area under the load–deflection curve | kN·mm |
| $a_0$ | Initial crack or notch depth | mm |
| b | Beam thickness | mm |
| E* | Effective Young's modulus of the concrete matrix | MPa |
| $F_s$ | Equivalent maximum fiber pull-out force used in the inverse analysis | N |
| h | Beam depth | mm |
| $K_{IC}$ | Mode-I fracture toughness of the concrete matrix | MPa·mm$^{0.5}$ |
| P | Applied load | kN |
| $P_{max}$ | Maximum load | kN |
| $V_f$ | Fiber volume fraction | % |
| $w_c$ | Critical crack opening corresponding to complete fiber pull-out | mm |
| δ | Mid-span beam deflection | mm |
| ΔA | Difference between the areas under the experimental and numerical load–deflection curves | kN·mm |
| $\Delta P_{max}$ | Difference between the experimental and numerical maximum loads | kN |
| λ | Span-to-depth ratio of the beam | – |
| ρ | Longitudinal steel reinforcement ratio | % |
| $\sigma_y$ | Yield strength of the longitudinal reinforcing steel | MPa |

## References

1. Vandewalle, L. Cracking behaviour of concrete beams reinforced with a combination of ordinary reinforcement and steel fibers. *Mater. Struct.* **2000**, *33*, 164–170. [CrossRef]
2. Dancygier, A.N.; Savir, Z. Flexural behavior of HSFRC with low reinforcement ratios. *Eng. Struct.* **2006**, *28*, 1503–1512. [CrossRef]
3. Meda, A.; Minelli, F.; Plizzari, G.A. Flexural behaviour of RC beams in fibre reinforced concrete. *Compos. Part B Eng.* **2012**, *43*, 2930–2937. [CrossRef]
4. Yoo, D.-Y.; Banthia, N.; Kang, S.-T.; Yoon, Y.-S. Size effect in ultra-high-performance concrete beams. *Eng. Fract. Mech.* **2016**, *157*, 86–106. [CrossRef]
5. Nguyen, D.-L.; Le, H.-V.; Vu, T.-B.-N.; Nguyen, V.-T.; Tran, N.-T. Evaluating fracture characteristics of ultra-high-performance fiber-reinforced concrete in flexure and tension with size impact. *Constr. Build. Mater.* **2023**, *382*, 131224. [CrossRef]
6. Kazemi, M.T.; Golsorkhtabar, H.; Beygi, M.H.A.; Gholamitabar, M. Fracture properties of steel fiber reinforced high strength concrete using work of fracture and size effect methods. *Constr. Build. Mater.* **2017**, *142*, 482–489. [CrossRef]

7. Nguyen, W.; Bandelt, M.J.; Trono, W.; Billington, S.L.; Ostertag, C.P. Mechanics and failure characteristics of hybrid fiber-reinforced concrete composites with longitudinal steel reinforcement. *Eng. Struct.* **2019**, *183*, 243–254. [CrossRef]
8. Hillerborg, A.; Modéer, M.; Petersson, P.-E. Analysis of crack formation and crack growth in concrete by means of fracture mechanics and finite elements. *Cem. Concr. Res.* **1976**, *6*, 773–782. [CrossRef]
9. Olesen, J.F. Fictitious crack propagation in fiber-reinforced concrete beams. *J. Eng. Mech.* **2001**, *127*, 272–281. [CrossRef]
10. Kang, S.-T.; Lee, Y.; Park, Y.-D.; Kim, J.-K. Tensile fracture properties of an ultra high performance fiber reinforced concrete (UHPFRC) with steel fiber. *Compos. Struct.* **2010**, *92*, 61–71. [CrossRef]
11. Kumar, B.; Sharma, A.; Ray, S. An analytical approach for characterizing the fracture behaviour of ultra-high-performance fibre reinforced concrete. *Compos. Struct.* **2024**, *332*, 117922. [CrossRef]
12. Yoo, D.-Y.; Banthia, N.; Yoon, Y.-S. Predicting the flexural behavior of ultra-high-performance fiber-reinforced concrete. *Cem. Concr. Compos.* **2016**, *74*, 71–87. [CrossRef]
13. Wille, K.; Kim, D.J.; Naaman, A.E. Strain-hardening UHP-FRC with low fiber contents. *Mater. Struct.* **2011**, *44*, 583–598. [CrossRef]
14. Fantilli, A.P.; Mihashi, H.; Vallini, P. Multiple cracking and strain hardening in fiber-reinforced concrete under uniaxial tension. *Cem. Concr. Res.* **2009**, *39*, 1217–1229. [CrossRef]
15. Abrishambaf, A.; Barros, J.A.O.; Cunha, V.M.C.F. Relation between fibre distribution and post-cracking behaviour in steel fibre reinforced self-compacting concrete panels. *Cem. Concr. Res.* **2013**, *51*, 57–66. [CrossRef]
16. Abrishambaf, A.; Barros, J.A.O.; Cunha, V.M.C.F. Tensile stress–crack width law for steel fibre reinforced self-compacting concrete obtained from indirect (splitting) tensile tests. *Cem. Concr. Compos.* **2015**, *57*, 153–165. [CrossRef]
17. Mudadu, A.; Tiberti, G.; Germano, F.; Plizzari, G.A.; Morbi, A. The effect of fiber orientation on the post-cracking behavior of steel fiber reinforced concrete under bending and uniaxial tensile tests. *Cem. Concr. Compos.* **2018**, *93*, 274–288. [CrossRef]
18. Zhang, J.; Stang, H.; Li, V.C. Experimental study on crack bridging in FRC under uniaxial fatigue tension. *J. Mater. Civ. Eng.* **2000**, *12*, 66–73. [CrossRef]
19. Vougioukas, E.; Papadatou, M. A model for the prediction of the tensile strength of fiber-reinforced concrete members, before and after cracking. *Fibers* **2017**, *5*, 27. [CrossRef]
20. Mujalli, M.A.; Dirar, S.; Mushtaha, E.; Hussien, A.; Maksoud, A. Evaluation of the tensile characteristics and bond behaviour of steel fibre-reinforced concrete: An overview. *Fibers* **2022**, *10*, 104. [CrossRef]
21. Rees, D.W.A.; Abdallah, S. Upper and lower bounds to pull-out loading of inclined hooked end steel fibres embedded in concrete. *Fibers* **2024**, *12*, 65. [CrossRef]
22. Hosseinmostofi, K.; Soltanzadeh, F.; Pereira, E.N.B. Orientation-dependent modeling of recycled steel fiber-reinforced self-compacting concrete. *Fibers* **2026**, *14*, 109. [CrossRef]
23. Stephen, S.J.; Raphael, B.; Gettu, R.; Jose, S. Determination of the tensile constitutive relations of fiber reinforced concrete using inverse analysis. *Constr. Build. Mater.* **2019**, *195*, 405–414. [CrossRef]
24. Matos, L.M.P.; Barros, J.A.O.; Ventura-Gouveia, A.; Calçada, R.A.B. A new inverse analysis approach for predicting the fracture mode I parameters of fibre reinforced concrete. *Eng. Fract. Mech.* **2021**, *246*, 107613. [CrossRef]
25. Sneha, S.; Kumar, B.; Ray, S. Notch sensitivity on post-cracking behaviour of ultra-high performance fibre-reinforced concrete. *Theor. Appl. Fract. Mech.* **2025**, *138*, 104925. [CrossRef]
26. Kumar, B.; Wang, C.; Liu, Y.; Zhou, S.; Ou, Q.; Liu, J.; Yu, Y.; Accornero, F.; Carpinteri, A. Scale effects investigation on the mechanical behaviour of steel-fibre and steel-bar (hybrid) reinforced concrete beams. In Proceedings of the 12th International Conference on Fracture Mechanics of Concrete and Concrete Structures (FraMCoS-12), Vienna, Austria, 23–25 April 2025.
27. Yoo, D.-Y.; Banthia, N. Mechanical properties of ultra-high-performance fiber-reinforced concrete: A review. *Cem. Concr. Compos.* **2016**, *73*, 267–280. [CrossRef]
28. Löfgren, I.; Stang, H.; Olesen, J.F. Fracture properties of FRC determined through inverse analysis of wedge splitting and three-point bending tests. *J. Adv. Concr. Technol.* **2005**, *3*, 423–434. [CrossRef]
29. Sousa, J.L.A.O.; Gettu, R. Determining the tensile stress–crack opening curve of concrete by inverse analysis. *J. Eng. Mech.* **2006**, *132*, 141–148. [CrossRef]
30. Mobasher, B.; Bakhshi, M.; Barsby, C. Backcalculation of residual tensile strength of regular and high-performance fiber-reinforced concrete from flexural tests. *Constr. Build. Mater.* **2014**, *70*, 243–253. [CrossRef]
31. Suárez, F.; Gálvez, J.C.; Alberti, M.G.; Enfedaque, A. Fracture and size effect of PFRC specimens simulated by using a trilinear softening diagram: A predictive approach. *Materials* **2021**, *14*, 3795. [CrossRef] [PubMed]
32. Carpinteri, A. A fracture mechanics model for reinforced concrete collapse. In *Proceedings of the IABSE Colloquium on Advanced Mechanics of Reinforced Concrete, Delft, The Netherlands, June 1981*; IABSE: Zürich, Switzerland, 1981; pp. 17–30.
33. Bosco, C.; Carpinteri, A. Discontinuous constitutive response of brittle matrix fibrous composites. *J. Mech. Phys. Solids* **1995**, *43*, 261–274. [CrossRef]
34. Carpinteri, A.; Accornero, F. The bridged crack model with multiple fibers: Local instabilities, scale effects, plastic shake-down, and hysteresis. *Theor. Appl. Fract. Mech.* **2019**, *104*, 102351. [CrossRef]

35. Carpinteri, A.; Accornero, F.; Rubino, A. Scale effects in the post-cracking behaviour of fibre-reinforced concrete beams. *Int. J. Fract.* **2023**, *240*, 1–16. [CrossRef]
36. Accornero, F.; Rubino, A.; Carpinteri, A. A fracture mechanics approach to the design of hybrid-reinforced concrete beams. *Eng. Fract. Mech.* **2022**, *275*, 108821. [CrossRef]
37. Ruiz, G.; Elices, M.; Planas, J. Experimental study of fracture of lightly reinforced concrete beams. *Mater. Struct.* **1998**, *31*, 683–691. [CrossRef]
38. Ruiz, G.; Ortega, J.J.; Yu, R.C.; Xu, S.; Wu, Y. Effect of size and cohesive assumptions on the double-K fracture parameters of concrete. *Eng. Fract. Mech.* **2016**, *166*, 198–217. [CrossRef]
39. Cucuzza, R.; Aloisio, A.; Accornero, F.; Marinelli, A.; Bassoli, E.; Marano, G.C. Size-scale effects and modelling issues of fibre-reinforced concrete beams. *Constr. Build. Mater.* **2023**, *392*, 131727. [CrossRef]
40. *GB/T 50081-2019*; Standard for Test Methods of Concrete Physical and Mechanical Properties. China Architecture & Building Press: Beijing, China, 2019.

**Disclaimer/Publisher's Note:** The statements, opinions and data contained in all publications are solely those of the individual author(s) and contributor(s) and not of MDPI and/or the editor(s). MDPI and/or the editor(s) disclaim responsibility for any injury to people or property resulting from any ideas, methods, instructions or products referred to in the content.